Journal of Alloys and Compounds 509 (2011) 8970–8977

Contents lists available at ScienceDirect

Journal of Alloys and Compounds

journal homepage: www.elsevier.com/locate/jallcom

High temperature thermoelectric properties and energy transfer devices of $Ca_3Co_{4-x}Ag_xO_9$ and $Ca_{1-y}Sm_yMnO_3$

Ling Han[a], Yang Jiang[a,*], Shanying Li[a], Huangming Su[a], Xinzheng Lan[a], Kaixuan Qin[a], Tingting Han[a], Honghai Zhong[a], Lei Chen[a], Dabin Yu[b,*]

[a] School of Materials Science and Engineering, Hefei University of Technology, Hefei, Anhui 230009, PR China
[b] State Key Laboratory of Pulsed Power Laser Technology, Electronic Engineering Institute, Hefei, 230037, PR China

ARTICLE INFO

Article history:
Received 2 December 2010
Received in revised form 29 June 2011
Accepted 29 June 2011
Available online 5 July 2011

Keywords:
Oxide thermoelectric materials
Self-ignition
Figures of merit
Thermoelectric devices
Maximum output power
Manufacturing factor

ABSTRACT

The high temperature oxide thermoelectric materials of p-type $Ca_3Co_{4-x}Ag_xO_9$ (denoted as p-Co349/Ag_x) and n-type $Ca_{1-y}Sm_yMnO_3$ (denoted as n-Mn113/Sm_y) were prepared by the self-ignition method combined with a sintering technique. The influence of doping Ag and Sm on the thermoelectric properties of the corresponding materials was evaluated. The figures of merit, ZT, for the p-Co349/$Ag_{0.2}$ and n-Mn113/$Sm_{0.02}$ materials reached maxima of 0.20 and 0.15 at 973 K, respectively. The performances of thermoelectric devices constructed with the p- and n-type pairs were evaluated in terms of the maximum output power (P_{max}) and manufacturing factor. The P_{max} and volume power density for the four-leg devices reached 36.8 mW and 81.9 mW cm^{-3} at ΔT of 523 K, respectively.

1. Introduction

As an important global issue of modern society, the growing energy crisis requires us not only to develop renewable and green energy but also to use the energy effectively and sufficiently. However, in industry production, more than 50% of energy is wasted in various forms without practical applications in any energy production process, mostly in the form of wasted heat. Because its sources are small and widely dispersed, the recycling of such a large quantity of wasted heat is difficult [1–3]. Fortunately, thermoelectric (TE) generation is one promising technology on the horizon that may solve these problems by converting heat energy directly into electric energy without the use of moving parts or the production of additional environmentally unfriendly waste [4–6]. Therefore, considerable efforts have been dedicated to the investigation of TE materials in the past decades. In comparison to conventional TE materials, such as Bi_2Te_3 [7–12] and PbTe [13–15] based alloys, high-temperature oxide TE materials, including $Ca_3Co_4O_9$ [16–20], $NaCoO_2$ [21–24], Li-doped NiO [25], $CaMnO_3$ [26–29], and $SrTiO_3$ [30], are of particular interest to researchers as a result of their high TE performance, nontoxic nature and high thermal and chemical stability.

In the family of high-temperature oxide thermoelectric materials, layered cobaltate structures of $Ca_3Co_4O_9$ and perovskite-type structures of $CaMnO_3$ have demonstrated promising thermoelectric properties and have become a hot topic in research. Yet, an improvement in the thermoelectric properties is strongly required for practical applications. One approach to improve the thermoelectric properties is optimisation of the material preparation technique and post treatment. In this regard, several methods have been developed to obtain improved thermoelectric properties [11,23,28,31–34]. For example, Lan et al. [28] reported a co-precipitation method to prepare fine-grained $CaMnO_3$-based ceramics with decreased thermal conductivity due to the enhancement of grain boundary scattering. In addition, it is worth pointing out that improved thermoelectric properties have been observed due to nanostructuring effects via different synthetic methods in recent years [9,10,34–37]. For example, through a nanocomposite approach using ball milling and hot pressing, a high peak ZT of 0.8 at 973 K was achieved out of p-type half-Heuslers by Yan et al. [34]. As an alternate approach, doping is another effective route for promoting thermoelectric properties. The improvements as a result of the doping may come from the variations in the carrier concentration, carrier mobility and thermal conductivity [6,19,24,38–40]. Tsai et al. [24] had systematically investigated the thermoelectric properties of Zn-doped $Na_{0.8}CoO_2$. The results showed that the doping Zn ions led to a decrease in the resistivity due to an improvement in the carrier mobility.

* Corresponding authors. Tel.: +86 551 2904358; fax: +86 551 2904358.
E-mail addresses: apjiang@hfut.edu.cn (Y. Jiang), dbyu@ustc.edu.cn (D. Yu).

0925-8388/$ – see front matter © 2011 Elsevier B.V. All rights reserved.
doi:10.1016/j.jallcom.2011.06.113

Until now, few attempts have been reported to improve TE performance by partial-substitution, including $Ca_{3-x}Na_xCo_4O_9$ [41] and $CaMn_{1-x}Nb_xO_3$ [32]. In this paper, p-type $Ca_3Co_{4-x}Ag_xO_9$ and n-type $Ca_{1-y}Sm_yMnO_3$ were prepared simply by the combination of a doping methodology and the self-ignition route. The addition of Ag to the layered structure $Ca_3Co_4O_9$ can effectively reduce the electrical resistivity (ρ) while retaining a relatively high Seebeck coefficient, consequently improving the thermoelectric power factor and the figure of merit ZT. For the $CaMnO_3$-based materials, although a high Seebeck coefficient is available, the thermoelectric performance is not satisfactory due to the inherent high electrical resistivity. In our work, to balance the relationship between the Seebeck coefficient and the electrical resistivity, Sm substitution at the Ca site has been employed to decrease the electrical resistivity and ultimately promote the comprehensive performance. To evaluate the potential for the practical application of thermoelectric materials, devices based on these two types of doped oxides were fabricated and characterised.

2. Experimental details

The powders of p-$Ca_3Co_{4-x}Ag_xO_9$ ($x = 0, 0.1, 0.2, 0.3$) and n-$Ca_{1-y}Sm_yMnO_3$ ($y = 0$, 0.02, 0.04, 0.06) were prepared by a self-ignition method reported previously by our group [22,23,32]. Analytically pure $Ca(NO_3)_2{\cdot}4H_2O$, $Co(NO_3)_2{\cdot}6H_2O$, $AgNO_3$, $Ca(NO_3)_2{\cdot}4H_2O$, $Mn(NO_3)_2{\cdot}4H_2O$, and $Sm(NO_3)_3{\cdot}6H_2O$ were used as the reagents for n- and p-type materials, respectively. Citric acid and stoichiometric amounts of relative nitrate hydrate for n- and p-type materials were completely dissolved in deionised water to prepare the individual solutions, respectively. During the heating and stirring process, the mixture became viscous gradually as a result of the formation of metal–citrate complex. When the temperature exceeded about 753 K, the mixture got combusted, yielding fine and black powder precursor. The two types of powder precursors were ground and calcined in air for 2 h at 1023 K for $Ca_3Co_{4-x}Ag_xO_9$ and 1173 K for $Ca_{1-y}Sm_yMnO_3$ to remove any residual substance. The resultant powders were pressed under 600 MPa using compacting dies. The p-type $Ca_3Co_{4-x}Ag_xO_9$ samples were sintered in air for 20 h at 1193 K, whereas the n-type $Ca_{1-y}Sm_yMnO_3$ samples were sintered in air for 10 h at 1473 K with a heating rate of 393 K h^{-1}.

Powder X-ray diffraction (XRD) was performed using CuKα radiation at room temperature with D/max-r_β equipment. The electrical resistivity (ρ) as a function of temperature for all the samples was measured from 573 K to 1073 K along the pressed plane by a standard DC four-terminal method. The Seebeck coefficient was calculated from the plot of the thermoelectric voltage against the temperature differential measured from 573 K to 973 K. The thermal conductivity $\kappa = \lambda C_p \rho$ was determined by the thermal diffusivity λ and specific heat capacity C_p, which were measured by the laser flash method taken on a TC-7000 (ULVAC). The morphology and structure of all the sample fracture surfaces were characterised by field emission-scanning electron microscopy (FE-SEM: SIRION 200, FEI, at 5 kV).

According to the thermoelectric performance of p-type and n-type materials, the devices were made of two pairs of $Ca_3Co_{3.8}Ag_{0.2}O_9$ (Co349/$Ag_{0.2}$) and $Ca_{0.98}Sm_{0.02}MnO_3$ (Mn113/$Sm_{0.02}$) for the p- and n-type legs to evaluate the transfer properties of heat to electricity. The p- and n-type bars were cut into legs with a height of 6 mm and cross-sectional area of 3 mm × 6 mm. The ends of the Co349/$Ag_{0.2}$ and Mn113/$Sm_{0.02}$ legs were grooved to increase the surface area. The assembly was placed between two alumina plates with dimensions of 15 mm × 20 mm × 0.6 mm, acting as hot and cold ends for relevant thermoelectric legs. By using Ag paste with 5 wt% $CaMnO_3$ (Mn113) oxide powder and Ag foils with a thickness of 0.02 mm, the Ag paste–Ag foil–Ag paste electrodes were made on the inner surface of Al_2O_3 substrate, which is pretreated by melting NaOH. Then the device was dried at 423 K and subsequently treated at 1073 K for 2 h to metallise the electrodes on the devices.

To evaluate the device performance, the top Al_2O_3 plate was heated to 923 K by a plate-shaped furnace at a heating rate of 300 K h^{-1}, while the bottom plate was held at 300 K by a copper block with circulated cooling water. The temperature differences between the hot and cold sides were measured by two digital κ-type thermocouples near the inner surface of the Al_2O_3 substrates. The temperature difference, ΔT, along the length of the devices is approximately equal to the difference in the interface temperatures between the hot alumina plate, T_{hot}, and the cold alumina plate, T_{cold}. The current–voltage lines and current–power curves of power generation were performed in air by sweeping the load resistance using an electronic load system, and then they were automatically recorded by a computer. To obtain all the electrical parameters of the devices, the measurements were also performed in an open circuit and short circuit mode under the same working conditions. The measurement of the thermoelectric voltage of the p- and n-legs over a range of applied temperature differences was conducted on the device working in open circuit mode. The corresponding thermoelectric Seebeck coefficient was directly deduced from the measured thermoelectric voltage. The resistivity (ρ) measurements were performed in a short circuit mode over a similar temperature gradient, in which the output leads of the devices were short-circuited.

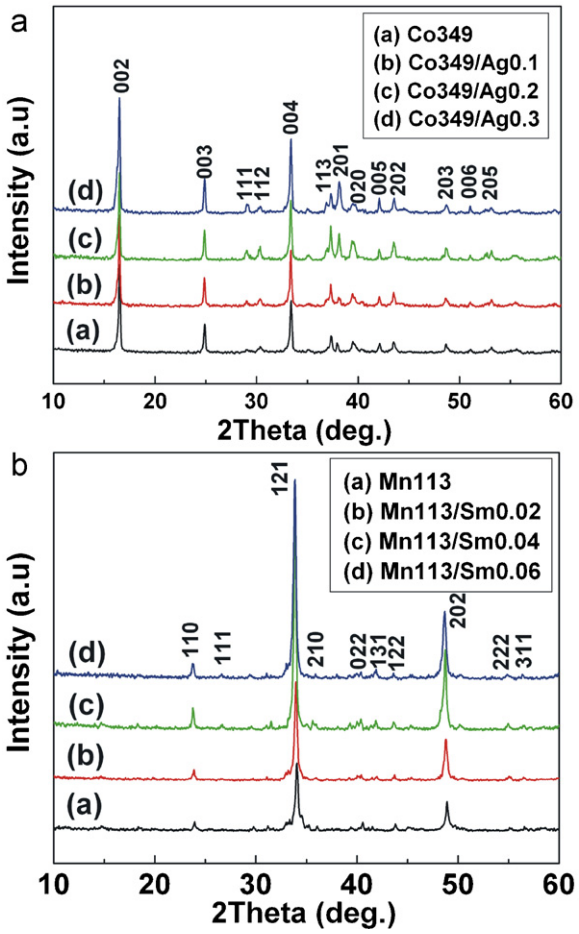

Fig. 1. (a) X-ray diffraction patterns of p-$Ca_3Co_{4-x}Ag_xO_9$ ($x = 0$, 0.1, 0.2, 0.3) materials, (b) X-ray diffraction patterns of n-$Ca_{1-y}Sm_yMnO_3$ ($y = 0$, 0.02, 0.04, 0.06) materials.

In an ideal case, $V_{0\text{-ideal}}$ is calculated by the sum of Seebeck voltage of p- and n-type materials, and the internal resistance R_{ideal} is calculated by the sum of the legs resistance. However, in real case, R_{in} is modified by the contact resistances leading to $R_{in} = R_{in\text{-ideal}} + R_{contact}$. The maximum output power ($P_{max} = V^2{}_{0\text{-ideal}}/4R_{in}$) could be obtained when the resistance load equals to the internal resistance of device ($R_{load} = R_{in}$). The manufacturing factor (MF), representing the cumulative influence of various factors of the fabrication process on the quality of the modules, is defined as $MF = P_{max}/P_{max\text{-ideal}}$ [42].

3. Results and discussion

Fig. 1(a) shows the X-ray diffraction patterns of oxide p-$Ca_3Co_{4-x}Ag_xO_9$ ($x = 0$, 0.1, 0.2, 0.3) materials. No impurity phases were observed. The X-ray diffraction patterns of n-$Ca_{1-y}Sm_yMnO_3$ ($y = 0, 0.02, 0.04, 0.06$) are presented in Fig. 1(b). All diffraction peaks could be attributed to $CaMnO_3$, indicating that no phase decomposition or reduction occurred during the sintering process. It is worth noting that all the diffraction peaks shifted to lower angles gradually with increasing doping Ag, which indicates that Ag has been doped into the $Ca_3Co_4O_9$ matrix. The ionic radius of Ag^{1+} and Co^{3+} are 1.15 Å and 0.65 Å, respectively. In this case, the cell parameter will increase accordingly in the presence of the doping Ag, which could account for the shift in the diffraction peak.

Fig. 2 shows the cross-section SEM fracture graphs of the p-$Ca_3Co_{4-x}Ag_xO_9$ samples of (a) Ag = 0.0 mol, (b) Ag = 0.1 mol, (c) Ag = 0.2 mol, and (d) Ag = 0.3 mol. Some layered morphology, cor-

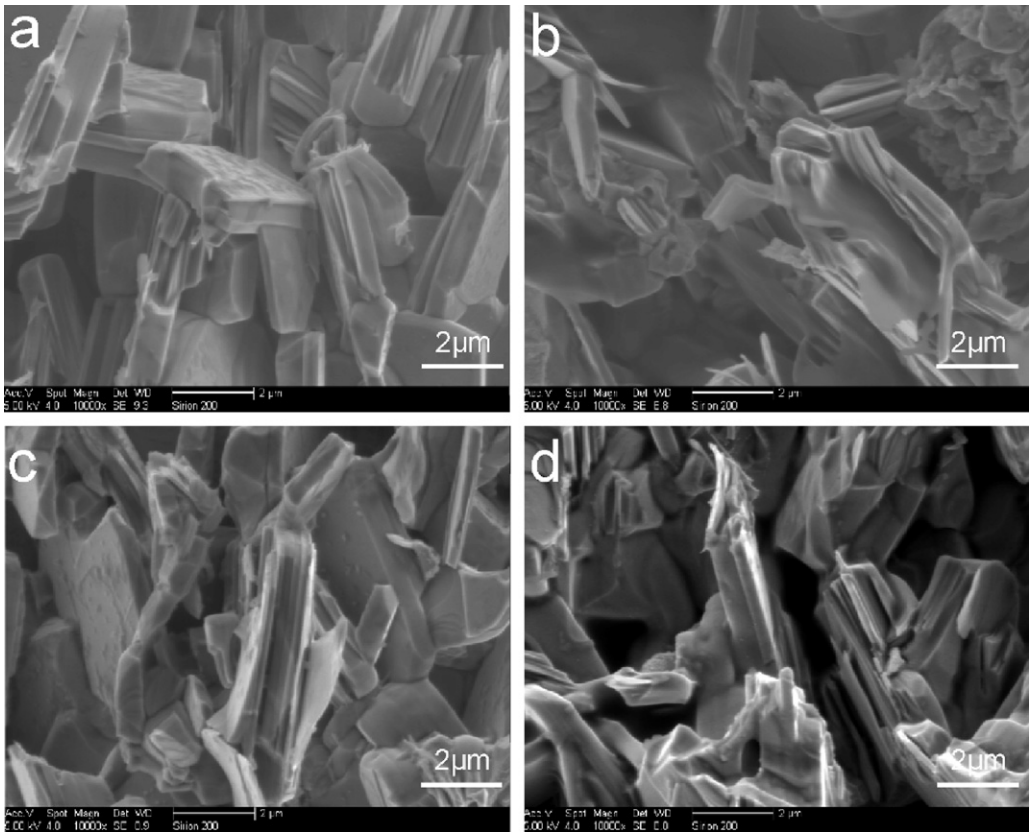

Fig. 2. Cross-section SEM fractographs of p-$Ca_3Co_{4-x}Ag_xO_9$ samples of (a) Ag = 0.0 mol, (b) Ag = 0.1 mol, (c) Ag = 0.2 mol, and (d) Ag = 0.3 mol.

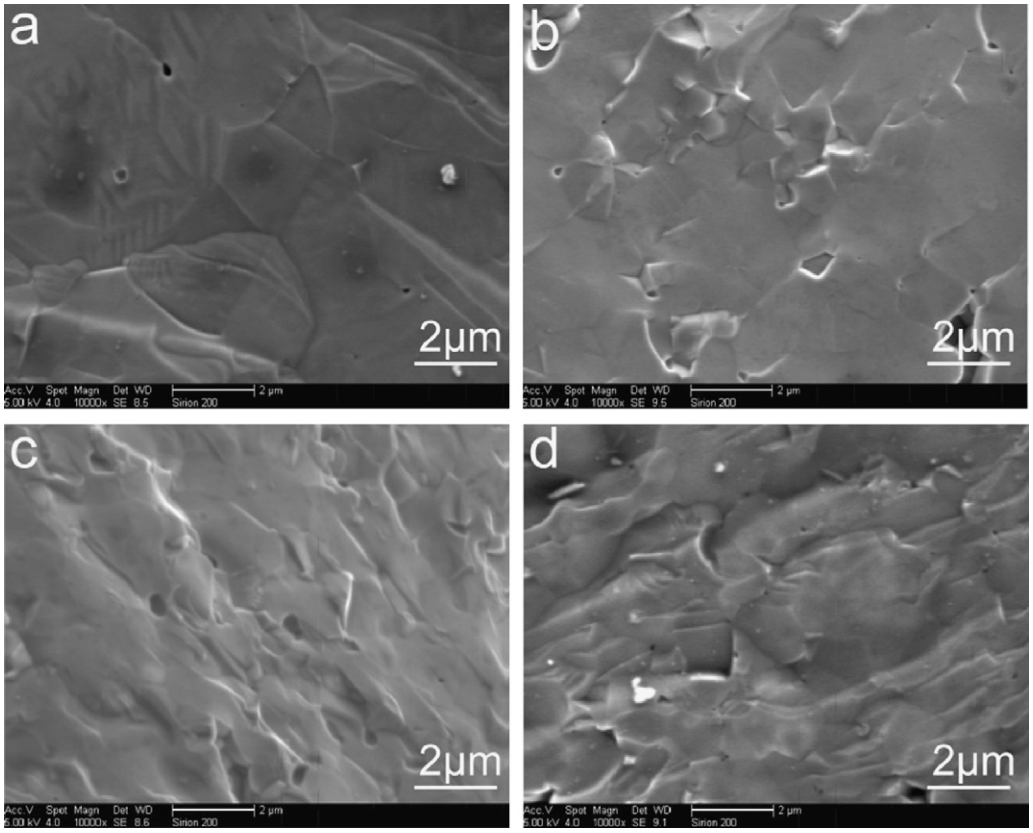

Fig. 3. Cross-section SEM fractographs of n-$Ca_{1-y}Sm_yMnO_3$ (y = 0, 0.02, 0.05, 0.1) samples of (a) y = 0 mol, (b) y = 0.02 mol, (c) y = 0.05 mol, and (d) y = 0.1 mol.

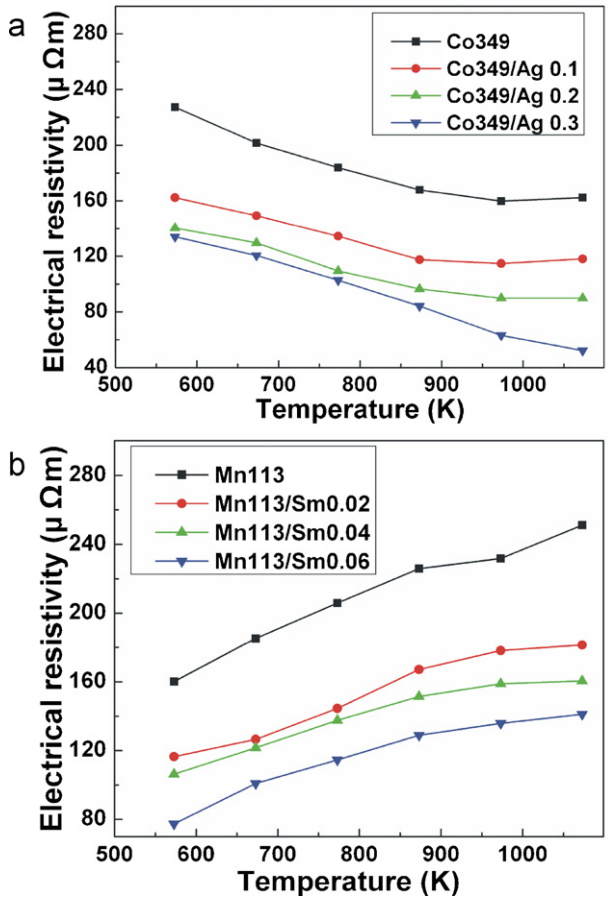

Fig. 4. The temperature dependences of the electrical resistivity (ρ) of p-$Ca_3Co_{4-x}Ag_xO_9$ (x = 0, 0.1, 0.2, 0.3) and n-$Ca_{1-y}Sm_yMnO_3$ (y = 0, 0.02, 0.04, 0.06) samples. (a) electrical resistivity (ρ) vs. temperature of p-$Ca_3Co_{4-x}Ag_xO_9$, (b) electrical resistivity (ρ) vs. temperature of n-$Ca_{1-y}Sm_yMnO_3$.

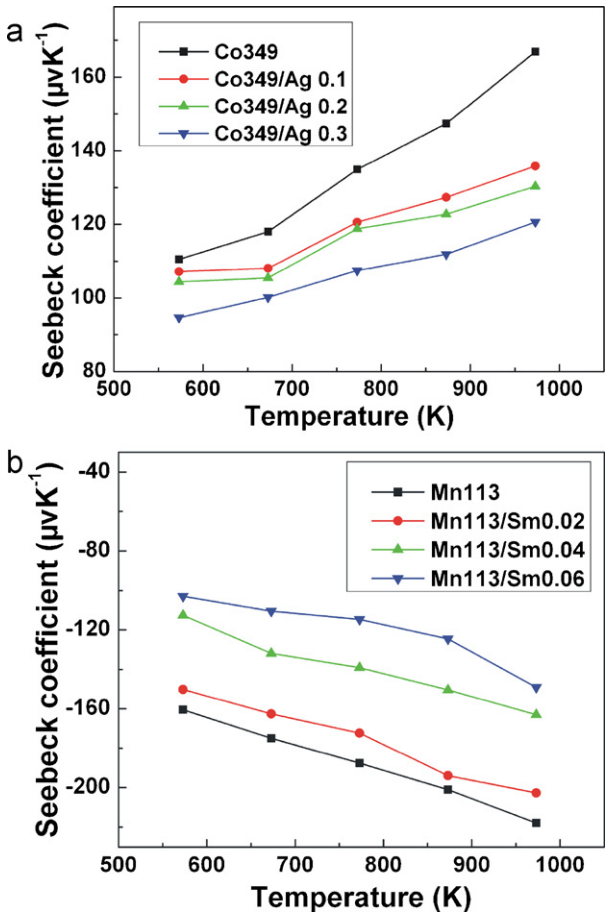

Fig. 5. The temperature dependence of the Seebeck coefficient of p-$Ca_3Co_{4-x}Ag_xO_9$ (x = 0, 0.1, 0.2, 0.3) and n-$Ca_{1-y}Sm_yMnO_3$ (y = 0, 0.02, 0.04, 0.06) samples. (a) Seebeck coefficient (S) vs. temperature of p-$Ca_3Co_{4-x}Ag_xO_9$, (b) Seebeck coefficient (S) vs. temperature of n-$Ca_{1-y}Sm_yMnO_3$.

responding to the intrinsic layered structure, can be observed. In addition, it can be seen that the fractured surfaces show homogeneous platelet-shaped grains.

Fig. 3 shows the cross-section SEM fracture graphs of the n-$Ca_{1-y}Sm_yMnO_3$ samples of (a) y = 0 mol, (b) y = 0.02 mol, (c) y = 0.05 mol, and (d) y = 0.1 mol. A few open pores appear at the boundaries of the grains in the sample, indicating that a compact texture was obtained. The fractured surfaces show uniform grains and high density.

In the Co349-layered oxide, the NaCl-type Ca_2CoO_3 layer and the electric conducting CoO_2 layer alternately stack along the c-axis [6]. The holes act as charge carrier in p-Co349/Ag_x, and the substitution of Ag for Co leads to an increase in the hole concentration [43]. The comprehensive electrical performance of all the p-$Ca_3Co_{4-x}Ag_xO_9$ and n-$Ca_{1-y}Sm_yMnO_3$ (573–1073 K) samples are shown in Fig. 4. As given in Fig. 4(a), the electrical resistivity for the p-Co349/Ag_x series (x = 0, 0.1, 0.2, 0.3) decreased with an increase in temperature, which is consistent with p-type semiconducting properties ($d\rho/dT$ < 0). Thus, at the same temperature, the resistivity decreased with an increase in Ag content. The temperature dependence of the resistivity could be ascribed to variation in the interface barrier at the boundary. As the temperature increases, the interfacial atoms are activated and tend to reconstruct the interface in a way that minimises the defect of the interface at the boundary, thus, favoring the carrier transfer.

Substituting the Ca site with a trivalent Sm cation increases the carrier concentration and generates Mn^{3+} cations in the Mn^{4+} matrix, changing the bending strength of the Mn–O–Mn bond

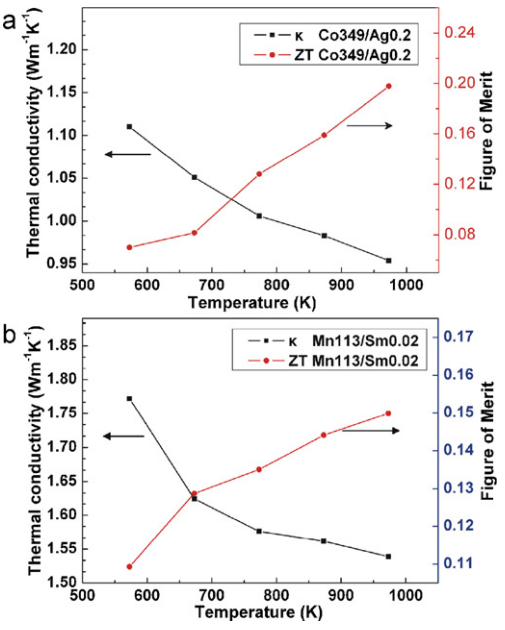

Fig. 6. The temperature dependence of thermal conductivity (κ) and figures of merit ZT of all the p-$Ca_3Co_{3.8}Ag_{0.2}O_9$ and n-$Ca_{0.98}Sm_{0.02}MnO_3$ samples. (a) Thermal conductivity (κ) and figure of merit ZT vs. temperature of p-$Ca_3Co_{3.8}Ag_{0.2}O_9$, (b) thermal conductivity (κ) and figure of merit ZT vs. temperature of n-$Ca_{0.98}Sm_{0.02}MnO_3$.

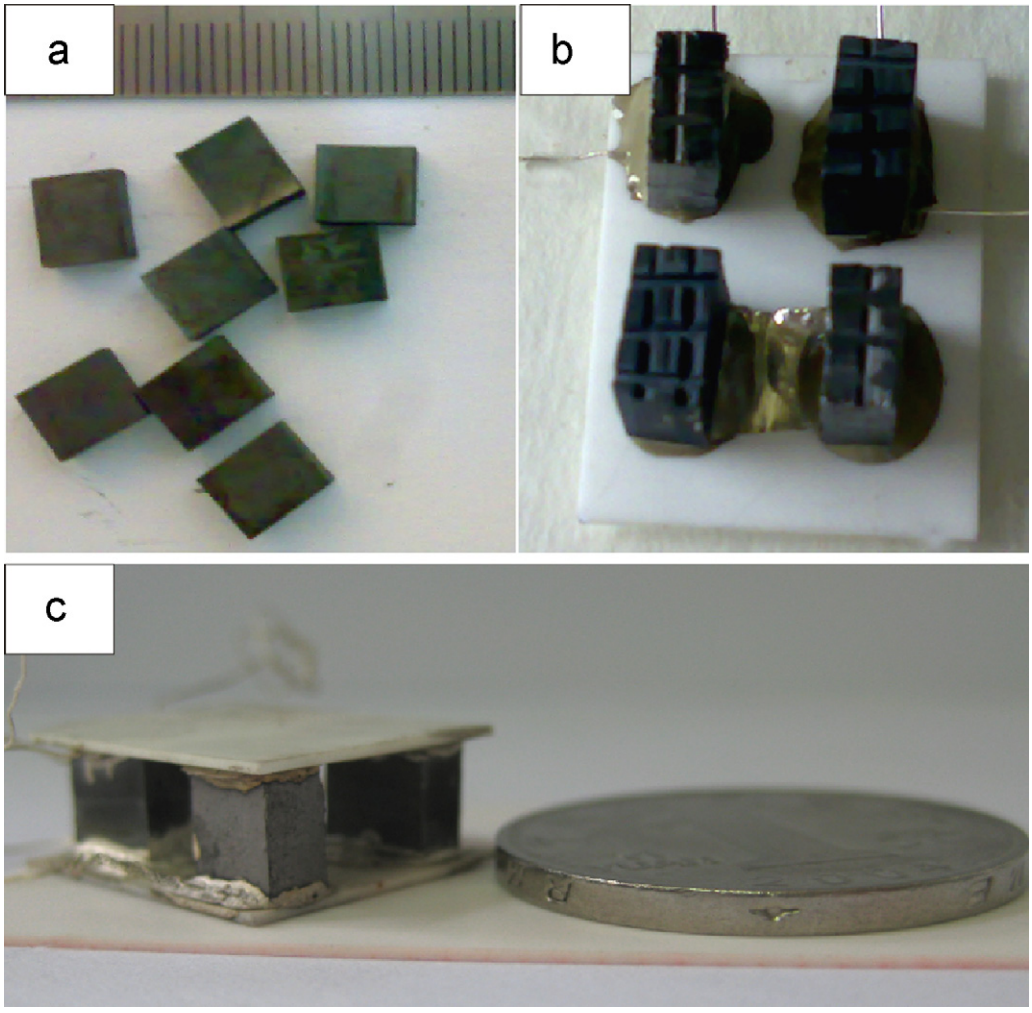

Fig. 7. The image of the oxide thermoelectric bulks and a device fabricated by p- and n-type oxide legs. (a) p-Co349/Ag_x and n-Mn113/Sm_y bulks, (b) grooving for the ends of the oxide legs, (c) shape of the four-legs Co349/$Ag_{0.2}$–Mn113/$Sm_{0.02}$ device vs. a coin.

[27]. In this case, the resistivity of all the n-Mn113/Sm_y samples decreases with the extent of the Sm substitution. The electrical resistivity of the individual components of n-Mn113/Sm_y increases as the temperature rises, which is consistent with previous reported results [27,44]. This temperature-dependent electrical resistivity could be ascribed to a decrease in the carrier mobility. The electrical resistivity is determined mostly by the carrier mobility and carrier concentration. Therefore, as the temperature increases, the thermal vibration of the lattice will be enhanced, and thus, phonon scattering will become evident and play a predominant role in the conductivity. Considering the carrier concentration, it mainly relies on the doping choice and its amount, and the concentration of the oxygen vacancy for oxide based materials. As for the electrical resistivity of the individual components of Mn113, the concentration of oxygen vacancies depends on the sintering conditions, including the atmosphere, the temperature and the time. The resistivity measurement was conducted on the sintered body. In this case, the concentration of the oxygen vacancy would approach being constant and thus might be neglected. Fig. 4(b) shows the resistivity variations of all the n-$Ca_{1-y}Sm_yMnO_3$ materials as a function of the temperatures ranging from 573 K to 1073 K. The resistivity presents a converse tendency with increasing Sm content. For perovskite structures of $CaMnO_3$, the electrons were regarded as the majority carriers. Meanwhile, impurity scattering becomes less significant at higher temperatures, resulting from the carriers moving faster and becoming less effectively scattered [45]. On the other hand, the impurities will be fully ionised, and accordingly, the carrier concentration will approach saturation. This may explain the relationship between the electrical resistivity and the temperature.

As shown in Fig. 5(a), the Seebeck coefficients (S) for the p-Co349/Ag_x samples remain positive, indicating p-type conductivity. Moreover, it should be noted that the value of S increased almost linearly with increasing temperature, while decreasing with the Ag-dopant content at high temperature. The relation between Seebeck coefficients and charge carrier concentration (n) can be expressed as $S = \gamma - \ln n$, where γ is the scattering factor [7]. At the same temperature, the scattering factor approaches being constant due to the intrinsic structure of misfit layers. On the other hand, the carrier concentration (n) increased with the rise in Ag content. Therefore, the Seebeck coefficients decrease with increasing Ag content. However, for the individual component of p-Co349/Ag_x, phonon scattering due to thermal vibration of the lattice atoms plays a more dominant role than that of the carrier concentration in determining the S of the sample with increasing temperature. Thus, the Seebeck coefficient (S) rises with increasing temperature.

As the temperature dependence of n-type Seebeck coefficients (S) suggests in Fig. 5(b), all the n-type compounds presented negative values throughout the investigated temperature zone,

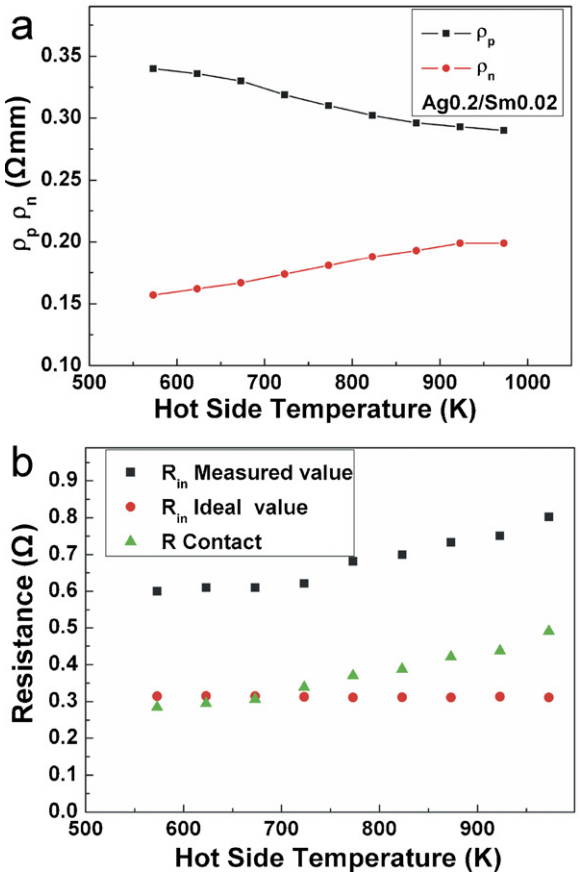

Fig. 8. The electrical performances of Co349/$Ag_{0.2}$–Mn113/$Sm_{0.02}$ device. (a) The resistivity (ρ) of Co349/$Ag_{0.2}$ and Mn113/$Sm_{0.02}$ vs. different hot side temperature, (b) R_{in_mea}, R_{in_ideal}, and $R_{contact}$ of Co349/$Ag_{0.2}$–Mn113/$Sm_{0.02}$ device vs. different hot side temperature.

indicating that the electrons are the majority carriers. The absolute values of S decreased with the addition of Sm, which is ascribed to the increase in the carrier concentration by substitution. On the other hand, the phenomenon of S for the individual component of n-Mn113/Sm_y increasing with temperature can be understood in terms of scattering, carrier concentration and carrier mobility, as mentioned in the discussion of the resistivity of n-Mn113/Sm_y.

The temperature dependence of thermal conductivity (k_{total}) and figures of merit ZT of p-Co349/$Ag_{0.2}$ and n-Mn113/$Sm_{0.02}$ are shown in Fig. 6(a) and (b). The k_{total} values of p-Co349/$Ag_{0.2}$ and n-Mn113/$Sm_{0.02}$ are 0.983 and 1.159 W m K^{-1} at 873 K, respectively, which are better than the previous report [46,47]. The k_{total} can be expressed by a sum of the lattice component (κ_L) and the electronic component (k_e), i.e., $\kappa_{total} = \kappa_L + \kappa_e$. In general, the values of κ_e show little fluctuation at high temperature. The decrease in κ_{total} could be attributed to the reduction of κ_L due to the increase in phonon scattering by substitution [32]. Analysing the variable electrical and thermal factors, the optimal figures of merit ZT for p-Co349/$Ag_{0.2}$ and n-Mn113/$Sm_{0.02}$ materials are 0.20 and 0.15 at 973 K, respectively. The figure of merit ZT and power factor (P) are the two main factors in thermoelectric device fabrication. Taking into account the as-obtained ZT, thermoelectric devices were prepared by p-Co349/$Ag_{0.2}$ and n-Mn113/$Sm_{0.02}$ to evaluate the output power and the power density.

The device shown in Fig. 7 was fabricated by optimising the manufacturing technology. The electrical resistivities at different hot side temperatures for p-Co349/$Ag_{0.2}$ and n-Mn113/$Sm_{0.02}$ legs were summarized in Fig. 8(a), which are higher than that for the starting materials (Fig. 4(a) and (b)). The increase in electrical resistivity can be attributed to a combined effect of semiconductor characteristic and the existing temperature gradient in device measurement [2]. Fig. 8(b) shows the temperature dependence of R_{in_mea}, R_{in_ideal}, and $R_{contact}$ for Co349/$Ag_{0.2}$–Mn113/$Sm_{0.02}$ device. To be clear, the internal resistance R_{in_mea} of the device corresponding to the slope of current-voltage lines were obtained directly by the measured system [48,49], and the R_{in_ideal} was calculated by the electrical resistivity of p- and n-type materials in different temperature gradient. In this case, $R_{contact}$ can be obtained by the formula $R_{contact} = R_{in\_mea} - R_{in\_ideal}$. Taking into account the relationship between $R_{contact}$ and P_{max}, the $R_{contact}$ may play a key role in the device power generation performance and therefore needs to be minimized. Power generation properties of the device at different temperatures by sweeping load resistance are presented in Fig. 9(a). The open circuit voltage (V_0), equal to the intercept of the current–voltage curve, reached 328 mV for a ΔT value of 523 K and a T_{hot} temperature of 873 K. The measured value of V_0 coincides well with the theoretical value ($V_{0\text{-ideal}}$) of 332 mV, calculated by the relation: $V_{0\_ideal} = n \times (S_P - S_N) \times \Delta T$ where $n = 2$ in a four-leg device, S_p and S_n are the Seebeck coefficient of the p- and n-legs, and ΔT is the temperature gradient between the hot and cold sides.

As the current-power curves shows in Fig. 9(a), the maximum output power (P_{max}) improved with increasing ΔT between the hot and cold sides of the device, which reached 12.9 mW, 17.4 mW and 36.8 mW with large ΔT of 330 K, 417 K and 523 K, respectively. In our work, the corresponding volume and mass power density at 873 K with a value of ΔT of 523 K are 81.9 mW cm^{-3} and 19.02 mW g^{-1}, respectively, and are presented in Table 1. Accord-

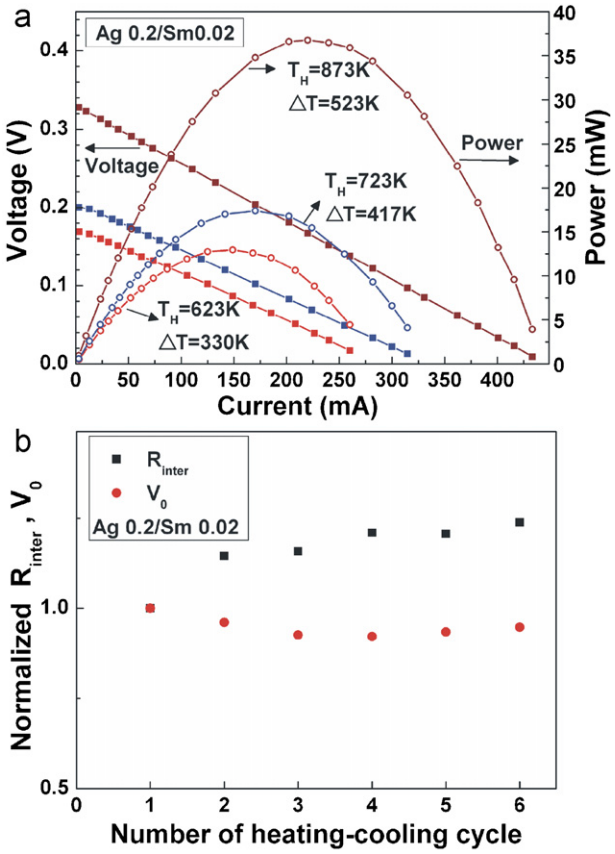

Fig. 9. The output performances of the Co349/$Ag_{0.2}$–Mn113/$Sm_{0.02}$ device. (a) Thermoelectric generation characteristics of the Co349/$Ag_{0.2}$–Mn113/$Sm_{0.02}$ device at hot-side temperature/temperature gradient of 623 K/330 K, 723 K/417 K, 873 K/523 K, (b) internal resistance (R_{in}) and open circuit voltage (V_0) of the device at T_{hot} of 873 K vs. the number of heating–cooling cycle test.

Table 1
Details of the physical parameters measured for the four-leg thermoelectric device.

Module type p/n	T_{hot} (K)	ΔT (K)	S_P ($\mu V K^{-1}$)	S_N ($-\mu V K^{-1}$)	V_0 (mV)	R_{in_ideal} (Ω)
Ag0.2/Sm0.02	873	523	123	194	328	0.43

R_{in} (Ω)	$R_{contact}$ (Ω)	P_{max_ideal} (mW)	P_{max} (mW)	Mass power density (mW g^{-1})	Volume power density (mW cm^{-3})	Manufacturing factor μ
0.73	0.3	63	36.8	19.02	81.9	0.583

ing to the results, the device of Co349/$Ag_{0.2}$–Mn113/$Sm_{0.02}$ worked successfully and stably at high temperature with a good thermoelectric performance, which showed considerably improved properties compared to the previous reports [2,42]. It is well known that the electrical contact and thermal contact play an important role in improving the device-manufacturing factor. In the present work, the manufacturing factor at a ΔT value of 523 K reached up to as high as 58.3% without using uniaxial pressure during manufacturing or testing process [47], which can be attributed to a drop in both the contact resistance and the difference of thermal expansion as mentioned above. In addition, the high-temperature durability is a non-negligible index of the device when operated at high temperatures. To investigate the high-temperature durability of the device, it was subjected to a heating–cooling cycle test from room temperature to 923 K, which was repeated six times in air. The measured open circuit voltage (V_0) and R_{in} at 873 K of the different cycles are given in Fig. 9(b). The values of V_0 and R_{in} at different cycles show little fluctuation, indicating that the fabricated device has good thermal durability.

4. Conclusions

The high-temperature oxide thermoelectric materials of p-$Ca_3Co_{4-x}Ag_xO_9$ ($x = 0$, 0.1, 0.2, 0.3) and n-$Ca_{1-y}Sm_yMnO_3$ ($y = 0$, 0.02, 0.04, 0.06) were prepared by a self-ignition method with a powder metallurgy technique. The thermoelectric properties, particularly the electrical resistivity and Seebeck coefficients, of p- and n-series materials were improved and optimised by our doping methods. The electrical resistivity for the p-Co349/Ag_x series decreased with an increase in the Ag content and the Seebeck coefficient decreased with the Ag dopant content at high temperature. As for all the n-Mn113/Sm_y samples, both the electrical resistivity and the Seebeck coefficient decreased with the extent of Sm substitution. The optimal figure of merit ZT for p-Co349/$Ag_{0.2}$ and n-Mn113/$Sm_{0.02}$ materials reaches 0.20 and 0.15 at 973 K, respectively. By using the doped oxides with the optimal ZT, four-leg thermoelectric devices of Co349/$Ag_{0.2}$–Mn113/$Sm_{0.02}$ were successfully prepared and characterised in terms of the maximum output power and the high-temperature durability. The devices could generate up to 36.8 mW, which corresponds to a volume power density of 81.9 mW cm^{-3} at ΔT of 523 K. Both the pretreatment of the substrate and the special design of the electrode structure of the Ag paste–Ag foil–Ag paste are demonstrated to be effective methods to promote device performance. The successful demonstration of good thermoelectric performances of the as-prepared modules suggests the great potential of these high-temperature doped oxide thermoelectric materials towards future applications.

Acknowledgements

We thank the financial supports of the National High Technology Research and Development Program of China (no. 2007AA03Z301), the Natural Science Foundations of China (nos. 20771032, 61076040, and 51072227) and Anhui Province (no. 070414200), National Basic Research Program of China (no. 2007CB9-36001), and Nippon Sheet Glass Foundation for Materials Science and Engineering (NSGF).

References

[1] T.M. Tritt, M. Subramanian, MRS Bull. 31 (2006) 188–198.
[2] E.S. Reddy, J. Noudem, S. Hebert, C. Goupil, J. Phys. D Appl. Phys. 38 (2005) 3751.
[3] Y. Lan, A.J. Minnich, G. Chen, Z. Ren, Adv. Funct. Mater. 20 (2010) 357–376.
[4] Service, Science 306 (2004) 806–807.
[5] H. Scherrer, S. Scherrer, in: D.M. Rowe (Ed.), CRC Handbook of Thermoelectrics, CRC Press, Boca Raton, FL, 1995, pp. 441–442.
[6] K. Koumoto, I. Terasaki, R. Funahashi, MRS Bull. 31 (2006) 206–210.
[7] J. Jiang, L. Chen, S. Bai, Q. Yao, J. Alloys Compd. 390 (2005) 208–211.
[8] X. Fan, J. Yang, W. Zhu, S. Bao, X. Duan, C. Xiao, K. Li, J. Phys. D Appl. Phys. 40 (2007) 5727.
[9] B. Poudel, Q. Hao, Y. Ma, Y. Lan, A. Minnich, B. Yu, X. Yan, D. Wang, A. Muto, D. Vashaee, Science 320 (2008) 634.
[10] J. He, J.R. Sootsman, S.N. Girard, J.C. Zheng, J. Wen, Y. Zhu, M.G. Kanatzidis, V.P. Dravid, J. Am. Chem. Soc. 132 (2010) 8669–8675.
[11] F. Li, X. Huang, Z. Sun, J. Ding, J. Jiang, W. Jiang, L. Chen, J. Alloys Compd. 509 (2011) 4769–4773.
[12] Y. Deng, H.-M. Liang, Y. Wang, Z.-W. Zhang, M. Tan, J.-I. Cui, J. Alloys Compd. 509 (2011) 5683–5687.
[13] K. Nouneh, I.V. Kityk, R. Viennois, S. Benet, K.J. Plucinski, S. Charar, Z. Golacki, S. Paschen, J. Phys. D Appl. Phys. 38 (2005) 965–973.
[14] T. Harman, P. Taylor, M. Walsh, B. LaForge, Science 297 (2002) 2229.
[15] J.Q. Li, S.P. Li, Q.B. Wang, L. Wang, F.S. Liu, W.Q. Ao, J. Alloys Compd. 509 (2011) 4516–4519.
[16] D. Wang, L. Chen, Q. Wang, J. Li, J. Alloys Compd. 376 (2004) 58–61.
[17] S. Bhattacharya, S. Rayaprol, A. Singh, A. Dogra, C. Thinaharan, D. Aswal, S. Gupta, J. Yakhmi, R.N. Kulkarni, S. Yusuf, J. Phys. D Appl. Phys. 41 (2008) 085414.
[18] T. Takeuchi, T. Kondo, T. Kitao, K. Soda, M. Shikano, R. Funahashi, M. Mikami, U. Mizutani, J. Electron Spectrosc. 144–147 (2005) 849–852.
[19] N.V. Nong, C.-J. Liu, M. Ohtaki, J. Alloys Compd. 509 (2011) 977–981.
[20] J. Pei, G. Chen, N. Zhou, D.Q. Lu, F. Xiao, Physica B: Condens. Matter 406 (2011) 571–574.
[21] I. Terasaki, Y. Sasago, K. Uchinokura, Phys. Rev. B 56 (1997) 12685–12687.
[22] W. Wang, Y. Jiang, M. Niu, L. Wang, B. Cao, Powder Technol. 184 (2008) 25–30.
[23] N. Li, Y. Jiang, G. Li, C. Wang, J. Shi, D. Yu, J. Alloys Compd. 467 (2009) 444–449.
[24] P.H. Tsai, T.S. Zhang, R. Donelson, T.T. Tan, S. Li, J. Alloys Compd. 509 (2011) 5183–5186.
[25] W. Shin, N. Murayama, K. Ikeda, S. Sago, J. Power Sources 103 (2001) 80–85.
[26] F.P. Zhang, X. Zhang, Q.M. Lu, J.X. Zhang, Y.Q. Liu, J. Alloys Compd. 509 (2011) 4171–4175.
[27] D. Flahaut, T. Mihara, R. Funahashi, N. Nabeshima, K. Lee, H. Ohta, K. Koumoto, J. Appl. Phys. 100 (2006) 084911.
[28] J. Lan, Y.-H. Lin, H. Fang, A. Mei, C.-W. Nan, Y. Liu, S. Xu, M. Peters, J. Am. Ceram. Soc. 93 (2010) 2121–2124.
[29] F.P. Zhang, Q.M. Lu, X. Zhang, J.X. Zhang, J. Alloys Compd. 509 (2011) 542–545.
[30] H. Ohta, K. Sugiura, K. Koumoto, Inorg. Chem. 47 (2008) 8429–8436.
[31] S. Katsuyama, Y. Takiguchi, M. Ito, J. Mater. Sci. 43 (2008) 3553–3559.
[32] L. Bocher, M. Aguirre, D. Logvinovich, A. Shkabko, R. Robert, M. Trottmann, A. Weidenkaff, Inorg. Chem. 47 (2008) 8077–8085.
[33] Y. Zhao, J.S. Dyck, B.M. Hernandez, C. Burda, J. Phys. Chem. C 114 (2010) 11607–11613.
[34] X. Yan, G. Joshi, W. Liu, Y. Lan, H. Wang, S. Lee, J.W. Simonson, S.J. Poon, T.M. Tritt, G. Chen, Z.F. Ren, Nano Lett. 11 (2011) 556–560.
[35] Y. Cao, T. Zhu, X. Zhao, X. Zhang, J. Tu, Appl. Phys. A – Mater. 92 (2008) 321–324.
[36] Y. Zhang, H. Wang, S. Kraemer, Y. Shi, F. Zhang, M. Snedaker, K. Ding, M. Moskovits, G.J. Snyder, G.D. Stucky, ACS Nano 5 (2011) 3158–3165.
[37] J.P. Heremans, C.M. Thrush, D.T. Morelli, Phys. Rev. B 70 (2004) 115334.
[38] H. Ihou-Mouko, C. Mercier, J. Tobola, G. Pont, H. Scherrer, J. Alloys Compd. 509 (2011) 6503–6508.
[39] T. Suzuki, M. Bahramy, R. Arita, Y. Taguchi, Y. Tokura, Phys. Rev. B 83 (2011) 035204.
[40] M. Liu, X. Qin, C. Liu, L. Pan, H. Xin, Phys. Rev. B 81 (2010) 245215.
[41] G. Xu, R. Funahashi, M. Shikano, Q. Pu, B. Liu, Solid State Commun. 124 (2002) 73–76.
[42] J. Noudem, S. Lemonnier, M. Prevel, E. Reddy, E. Guilmeau, C. Goupil, J. Eur. Ceram. Soc. 28 (2008) 41–48.
[43] M. Mikami, N. Ando, R. Funahashi, J. Solid State Chem. 178 (2005) 2186–2190.

[44] M. Ohtaki, H. Koga, T. Tokunaga, K. Eguchi, H. Arai, J. Solid State Chem. 120 (1995) 105–111.
[45] S.M. Sze, Semiconductor Devices: Physics and Technology, second ed., John Wiley & Sons, New York, 2001, p49.
[46] S. Li, R. Funahashi, I. Matsubara, K. Ueno, S. Sodeoka, H. Yamada, Chem. Mater. 12 (2000) 2424–2427.
[47] Y. Masuda, D. Nagahama, H. Itahara, T. Tani, W.S. Seo, K. Koumoto, J. Mater. Chem. 13 (2003) 1094–1099.
[48] R. Funahashi, S. Urata, K. Mizuno, T. Kouuchi, M. Mikami, Appl. Phys. Lett. 85 (2004) 1036–1038.
[49] S. Lemonnier, C. Goupil, J. Noudem, E. Guilmeau, J. Appl. Phys. 104 (2008) 014505.